Microplastics detection in agricultural soil combining 3D Laser Scanning Confocal Microscopy with machine learning

Tabea Scheiterlein, Peter Fiener

Angaben zur Veröffentlichung / Publication details:

Scheiterlein, Tabea, and Peter Fiener. 2026. "Microplastics detection in agricultural soil combining 3D Laser Scanning Confocal Microscopy with machine learning." *Microplastics and Nanoplastics* 6 (1): 47. https://doi.org/10.1186/s43591-026-00202-8.

Microplastics and Nanoplastics

RESEARCH

Open Access

Microplastics detection in agricultural soil combining 3D Laser Scanning Confocal Microscopy with machine learning

Tabea Scheiterlein[1*] and Peter Fiener[1]

Abstract

Accurate quantification of microplastics (MPs) in soils remains analytically challenging due to complex mineral and organic soil matrices. Microscopy, spectroscopy and thermoanalytical techniques are widely applied to analyse MPs in soils. However, integrated workflows enabling simultaneous assessment of quantitative surface properties remain limited. Surface roughness and complexity may influence particle-environment interactions and are therefore relevant for understanding the environmental behaviour of MPs. This study developed and evaluated an oxidative- and corrosive-substance-free workflow for the simultaneous assessment of MP abundance, size, shape, and quantitative surface roughness and complexity in agricultural soils. The workflow combines density separation with freezing, 3D Laser Scanning Confocal Microscopy (3D LSCM; Keyence VK-X1000, Japan) and machine-learning-based automated detection. In addition to enabling time-efficient particle classification, machine-learning integrates multi-layer 3D LSCM outputs, including height, laser reflection, and colour (RGB) information. Data acquisition was performed at a $pixel_{xy}$ size of 2.7 µm and a height pitch of 4 µm. The method was evaluated using three agricultural topsoils spiked with transparent and black low-density polyethylene and polypropylene fragments (< 53 µm, 53–100 µm, 100–250 µm) and polypropylene fibres (1000 µm length). MPs ≥ 53 µm were reliably detected with a mean recovery of 80% ± 28% in soils with low to medium particulate organic matter content (POM). As expected, detection performance decreased in soils with high POM content, as POM was not removed during sample preparation, which made it particularly difficult to determine black MPs and fibres. Up to four 25 g samples can be processed and analysed within three days, enabling time-efficient MP (≥ 53 µm) assessment in agricultural soils and complementing established analytical approaches through quantitative surface characterisation.

Keywords Microplastic, Soil, Surface analyses, 3D Laser Scanning Confocal Microscopy, Machine learning, Freezing

*Correspondence:
Tabea Scheiterlein
tabea.scheiterlein@geo.uni-augsburg.de

Full list of author information is available at the end of the article

Graphical abstract

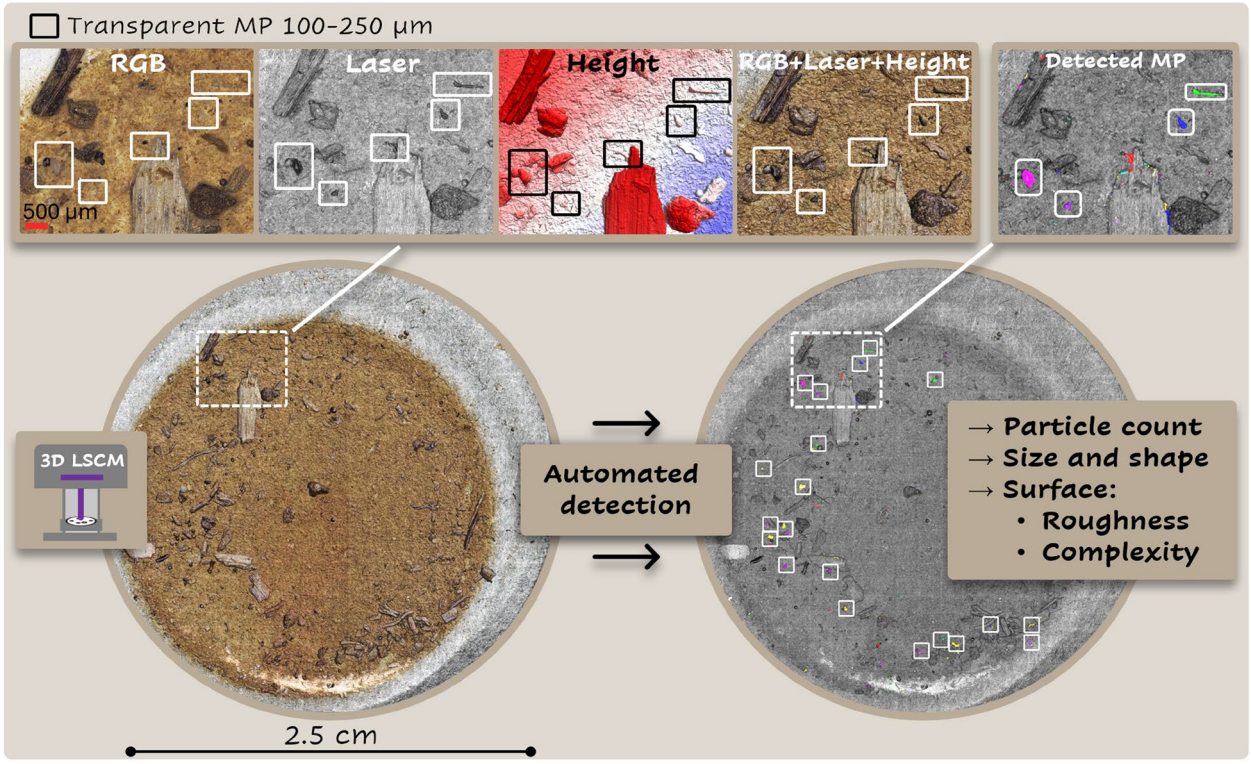

Introduction

Soils are considered one of the most important terrestrial sinks for microplastics (MPs) [1], defined as plastic particles and fibres ranging of 1–5000 µm [2]. MPs enter soils through a multiple pathways, including tyre abrasion along streets [3–5], paint fragments [6, 7], litter fragmentation [8–10] and atmospheric deposition [11–13]. In agricultural soil systems additional sources need to be considered. These comprise fragments of plastic material used in agriculture [9, 14–16], such as black mulch films, transparent greenhouse tunnels and silage bags [17, 18], which are widely applied to enhance productivity and are often discussed in the context of achieving the United Nations Sustainable Development Goals (SDGs) [19]. In addition, the application of organic fertilisers, including compost and sewage sludge, may transfer MPs originating from waste management and wastewater systems into agricultural soils [20–23]. Together, these inputs contribute to the accumulation of MPs in agricultural soils [9, 22, 24].

MPs might affect soil physical properties (e.g., aggregation and soil water fluxes) [25, 26], as well as chemical and biological soil properties (e.g., bacterial communities, soil fauna, and rhizosphere) [27–29], which stands in contrast to the SDGs. Beyond MP polymer identity and concentration, morphological parameters such as size, shape, volume, and surface complexity in terms of surface area are key factors in ecotoxicological risk assessment for soil invertebrates [30]. Surface roughness and complexity may influence particle-soil interactions, adhesion processes [31–34]. Quantitative assessment of these parameters is therefore essential for understanding MP behaviour in soils.

Considerable efforts have therefore been directed towards the extraction, quantification, and characterisation of MPs in complex sample materials such as soil. Thermoanalytical techniques such as pyrolysis-gas chromatography-mass spectrometry (Pyr-GC-MS) [35] and thermal extraction desorption-gas chromatography-mass spectrometry (TED-GC-MS) [4, 36] provide rapid polymer identification and mass quantification. Microscopic imaging [37, 38] enables particle-resolved information on abundance, size, shape and colour [39]. Microscopy in combination with spectroscopic methods such as µ-Fourier transform infrared spectroscopy (µ-FTIR) [40, 41], µ-Raman spectroscopy (µ-Raman) [42], and attenuated total reflectance-FTIR (ATR-FTIR) [15, 41] allows additional polymer-specific identification [43–45]. These approaches provide complementary information; however, they are rarely integrated with quantitative three-dimensional surface analysis.

Several additional analytical restrictions remain. With fluorescence microscopy, μ-FTIR, and μ-Raman it is challenging to detect black or dark-coloured MPs, especially if soil organic matter (SOM) is present in the samples [37, 43, 46, 47]. Transparent MPs may be overlooked during stereomicroscopic inspection [40, 48] or preselection [47]. Moreover, most analytical approaches use corrosive and oxidative substances during sample preparation, such as zinc chloride, hydrogen peroxide and/or the Fenton reaction [44], which may alter the MP size and surface properties, or cause further fragmentation [40, 49, 50].

MP surface properties have been qualitatively investigated using Scanning Electron Microscopy (SEM) [51–54] to complement thermoanalytical and spectroscopic techniques. Quantitative analyses of surface complexity and roughness in soils remain limited. Micro-X-ray computed tomography (micro-CT) and nano-X-ray computed tomography (nano-CT) have been used to determine surface complexity in terms of surface area and porosity (volume-pore-ratio) of plastic fruit stickers in compost [21]. Yet, such 3D surface characterisation is not routinely integrated into MP-soil workflows.

In addition, heterogeneous MP background contamination in soils [44, 55] requires the analysis of representative sample masses [44], increasing processing time due to sample preparation, measurement time [43], and (semi-)manual data analysis [56]. Automated data analysis, therefore, represents a crucial step towards efficient workflows [56]. Machine-learning-based data analysis enables an automated detection and, further, the integration of multi-layer datasets, including 2D morphological features [3] and spectral features [57, 58]. However, the systematic integration of machine learning with 3D surface-resolved MP detection in soils remains limited. Further for reproducible applications in the future, more training data and the availability of the programming code are needed [56].

To date, no method can fully capture all aspects of MP polymer identification, abundance, mass, particle size, shape, and surface properties within one analytical workflow. Consequently, analytical techniques must be selected according to the specific research question. There is a need for approaches that preserve MP morphology during sample preparation and enable detection across diverse MP characteristics in presence of SOM. Such approaches should also reduce (semi-)manual data analysis and complement established thermoanalytical and spectroscopic techniques. In addition, analytical approaches enabling the quantitative assessment of MP surface complexity and roughness in contaminated soils is still rarely integrated into routine workflows.

This study developed and evaluated a novel workflow for automatic MP detection in agricultural soil using 3D Laser Scanning Confocal Microscopy (3D LSCM, VX-K 1000, Keyence, Japan) combined with machine-learning-based analysis integrating colour (RGB), laser reflection, and 3D surface features. Specifically, we aim to develop a method that: (i) preserve morphology during sample preparation without oxidative and corrosive substances; (ii) enable detection of small MP particles (11–250 μm) and fibres (~1000 μm length) in the presence of SOM; (iii) quantify the MP in abundance, size, 3D shape, volume and surface properties (complexity and roughness values); and (iv) facilitate time-efficient cost-conscious processing of representative soil sample masses compared with workflows requiring extensive SOM purification and (semi-)manual data analysis.

The research focuses on prevalent light-density polymers (LDPE and PP) [59], which are commonly used in plasticulture [18], and on MPs in transparent and black colour classes that may be underrepresented in routine detection approaches [60]. The approach was evaluated on three spiked agricultural topsoils containing MPs of varying size classes (≤53 μm, 53–100 μm, 100–250 μm), surface conditions (virgin and weathered), and shapes (fragments and fibres; ~1000 μm length). We hypothesised that (H1) the corrosive-substance-free sample preparation preserves MP morphology, particularly surface complexity; (H2) robust MP detection is achievable in agricultural soils despite the presence of SOM, with an expected decreasing performance at higher particulate organic matter (POM) contents and smaller MP particle sizes; and (H3) MPs can be distinguished from soil particles primarily using size-independent morphological and surface descriptors.

Materials and methods

Cross-contamination prevention

The MP extraction was carried out in a laminar flow box (FBS 93-SuSi, Spectec, Germany). Cotton lab coats were worn during sample preparation, measurement and equipment cleaning. Whenever samples were moved within the laboratory, they were always covered with a stainless-steel lid or kept in a glass Petri dish and only uncovered during the 3D LSCM analysis. In this study, the use of hazardous substances was avoided; hence, neither a fume hood nor laboratory gloves were required. All samples were handled with tweezers or a spatula. The equipment was thoroughly cleaned between uses, following an internal standardised procedure that included rinsing with ultrapure water (Elga-Veolia Purelab Flex 2, Germany), washing with 96% ethanol, and heating to 140 °C.

Table 1 Overview of soil properties presented in mean ± standard deviation

Properties	Soil 1 (S1)	Soil 2 (S2)	Soil 3 (S3)
Site	Dudenhofen (West Germany)	Strass (Southern Germany)	Freising (Southern Germany)
Depth [cm]	0–20	0–5	0–5
Sand [%]	86.6 ± 1	72.0 ± 0	16.0 ± 0
Silt [%]	9.7 ± 1	17.5 ± 0.7	60.0 ± 1.4
Clay [%]	3.7 ± 1	10.5 ± 0.7	24.0 ± 1.4
SOC [%]	0.58 ± 0.05	1.01 ± 0.06	1.27 ± 0.11
$CaCO_3$ [%]	< 1	< 1	0.14 ± 0.02
N [%]	0.06 ± 0.02	0.12 ± 0.01	0.16 ± 0.01
pH_{CaCl2} [%]	4.6 ± 0.1	6.9 ± 0.14	7.1 ± 0.28
POM	high	low to medium	low to medium

Soil texture acquired from sieve-pipette method; soil organic carbon (SOC), calcic carbonate ($CaCO_3$), nitrogen (N) after elementary analyses; pH in 0.01 mol calcic chloride ($CaCl_2$) soil elute; and particulate organic matter (POM) was qualitatively analysed (Fig. SI1). Soil properties of S1 were provided by LUFA Speyer, Germany and those of S2 and S3 were provided by the Bavarian state environmental agency (LFU), Germany

Table 2 Properties and size class of the 10 different microplastics (MPs) used for spiking

Size class [µm]	Polymer	Colour	Shape	Characteristic	MP-type
1000	PP	white/transparent	fibre	virgin	1
100–250	PP	transparent	particle	weathered fragment	2
	LDPE	transparent		film fragment	3
	LDPE	black		film fragment	4
53–100	PP	transparent	particle	weathered fragment	5
	LDPE	transparent		film fragment	6
	LDPE	black		film fragment	7
< 53	PP	transparent	particle	weathered fragment	8
	LDPE	transparent		film fragment	9
	LDPE	black		film fragment	10

The MP either consist of light density polyethylene (LDPE) or polypropylene (PP)

Test materials

Soil

Three different agricultural topsoils representing different regions and textures in Germany were used (Table 1). Soil 1 (S1) is a sandy soil with high POM, obtained as a commercial standard soil (LUFA 2.1; LUFA Speyer, Germany) sampled from Dudenhofen (Western Germany) from a depth of 0–20 cm. LUFA soils originate from agricultural land, where neither pesticides nor organic fertiliser (except green manure) were applied for at least four years prior to sampling; mineral fertilisers were applied no later than three months before sampling. Soil 2 (S2) is a sandy soil with low to medium POM, sampled in Strass (Southern Germany) from a depth of 0–5 cm. Soil 3 (S3) is a silty soil with low to medium POM, sampled in Freising (Southern Germany) from a depth of 0–5 cm. S2 and S3 originated from intensive, long-term agriculture with a typical regional crop rotation and without plasticulture. S1 was under agricultural use for several decades but has been left uncultivated for at least four years prior to sampling, which is probably the reason for its higher POM content. S2 and S3 were air dried (20 °C) for five days in aluminium boxes in a separate sample storage room and mixed daily to ensure homogenous drying. S1 was delivered pre-dried and packed in a white/transparent plastic bag (woven outer layer, inner film layer). All soils were manually closed-sieved to < 2 mm and subdivided into 25 g samples. To ensure reproducible and representative subdivision for the controlled spiking experiment, an automated rotary sample divider (PT 100, Retsch, Germany) was used. To minimise potential cross-contamination, the sample divider was thoroughly cleaned with 96% ethanol and compressed air before initial use and between processing of soils S1, S2, and S3. The 25 g soil samples were stored in covered glass jars until the spiking procedure. S1 showed substantially higher visible POM content compared to S2 and S3, whereas S3 exhibited the highest soil organic carbon (SOC) and clay content (Table 1). POM was qualitatively assessed following the MP extraction procedure after density separation and freezing (Figure SI1).

Microplastics

Ten MP types representing plasticulture sources, including mulching films, greenhouse films, and non-woven textiles were used (Table 2; Fig. SI2). Fibres additionally represent MPs transferred from other systems. These materials included: (i) commercially available transparent LDPE particles (LDPE-T; LDPE 140 and LDPEXF 1040, Fixatti AG, Germany); (ii) predominant transparent PP particles (PP-T) derived from ocean-sourced material manufactured to MPs; (iii) commercially available black LDPE agricultural film cryomilled to MP (LDPE-B); (iv) commercially available transparent/white PP fibres (F PP 264, Schwarzwälder Textil-Werke, Germany) with a length of ~ 1000 µm. The LDPE material has a density of $\rho = 0.91–0.92$ g cm^{-3} and PP of $\rho = 0.90–0.92$ g cm^{-3}. All particle types except fibres were separated into three size classes (< 53 µm, 53–100 µm, and 100–250 µm) using closed dry sieving. PP-T particles were irregularly shaped fragments and represent MPs with a weathered surface. LDPE-T and LDPE-B particles were irregularly shaped film fragments, which could also appear in a fibrous shape.

Spiking procedure

In the following, the MP material used for soil spiking (MP_{spik}) and the MPs detected after extraction and analysis (MP_{det}) are distinguished to enable recovery calculation, similarity analysis, and surface alteration assessment in subsequent method evaluation (Sect. "Method evaluation"). The mass of MP_{spik} added to each soil sample was determined using a microbalance (XP6 Micro Balance, Mettler Toledo, Switzerland). For particle fractions, the following target masses were applied: 0.05 mg (100–250 µm), 0.02 mg (53–100 µm), and 0.01 mg (< 53 µm). For PP fibres (~ 1000 µm length), 0.10 mg was used. These correspond to nominal MP-soil mass concentrations (w/w) of 2 ppm (100–250 µm), 0.8 ppm (53–100 µm), 0.4 ppm (< 53 µm), and 4 ppm (fibres), respectively.

Prior to soil spiking, MP_{spik} was characterised using the 3D LSCM to determine size distribution, particle volume and surface properties. Quantified particle volume (Table SI5) in combination with the known polymer densities, were used to establish a statistical mass-to-particle conversion. This conversion served as the basis for calculating particle numbers from the applied mass (Sect. "Mass-to-particle count conversion") and for determining recovery rates of MP_{det} (Sect. "Statisitcal recovery rate"). Furthermore, the surface descriptors of MP_{spik} provided the morphological reference for subsequent comparison with MP_{det}. This comparison enabled similarity analysis (Sect. "Similarity analysis") and evaluation of potential surface alteration induced by mechanical dispersion and separation steps (Sect. "Microplastic alteration control"). For spiking 25 g of soil were transferred from the glass jars into a 500 ml stainless-steel centrifugation tube (Tube 13507, Sigma Laborzentrifugen GmbH, Germany) and the respective MP_{spik} material was added.

In total, 30 different MP-soil combinations (10 MP types x 3 soils) were prepared and analysed in triplicate, resulting in 90 spiked samples. In addition, three soil blanks and 10 MP blanks were included, yielding 103 test samples. MP blanks (MP + ultra-pure water) were used to assess method performance without soil and to monitor laboratory background contamination. Soil blanks (soil without MP addition) were analysed to determine initial MP background levels and potential contamination during soil preparation.

Microplastic extraction

A three-step procedure was applied to extract MPs from soil < 2 mm. This workflow was optimised for parallel laboratory processing of up to four independent 25 g samples (100 g total), per extraction batch, on the laboratory setup and centrifugation capacity (Fig. 1A). The samples

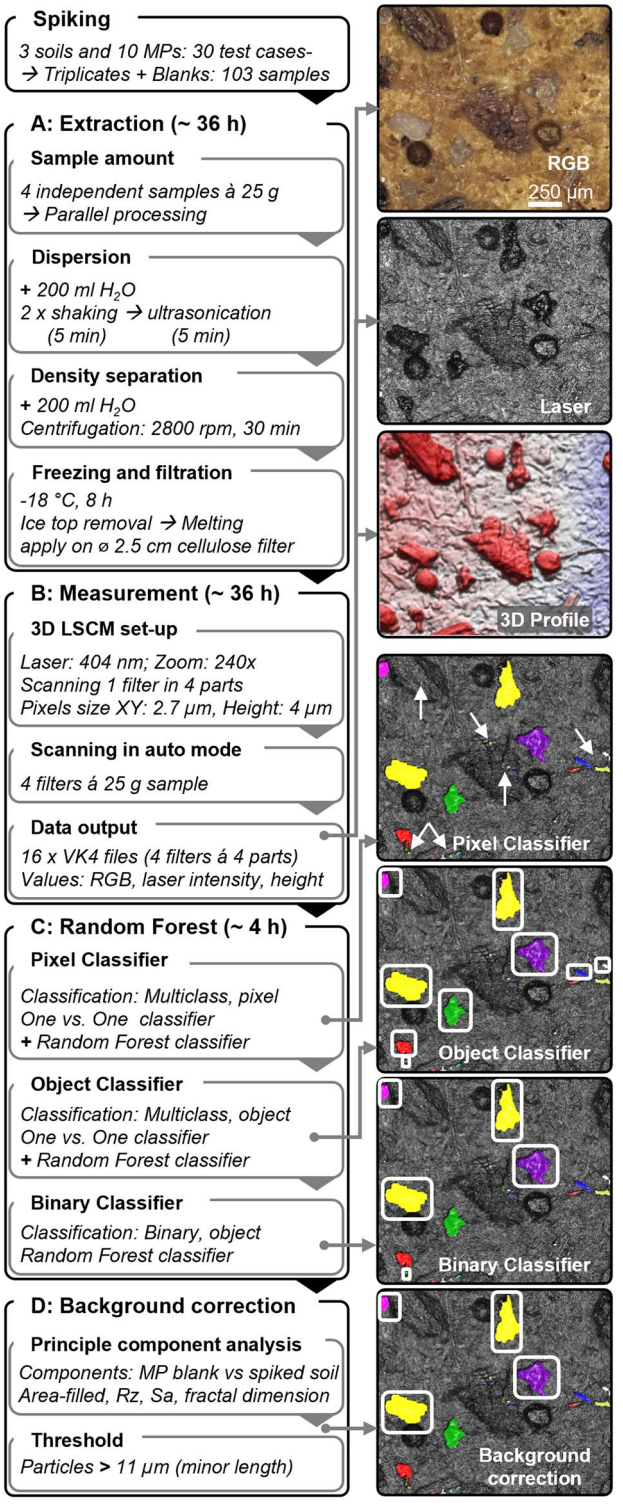

Fig. 1 Workflow (**A**–**D**, left) and 3D Laser Scanning Confocal Microscope (3D LSCM) output with data analysis (right) for transparent low-density polyethylene (100–250 µm) in silty soil with low to medium particulate organic matter (S3). Transparent microplastics (MPs) appear black in the laser intensity image; height ranges from low (blue) to high (red). Pixel Classifier results are colour-coded (arrows: false positives); final MP detections are marked by white rectangles

were processed in 500 ml stainless-steel centrifugation tubes (Fig. SI3A).

(i) **Dispersion**: For physical soil aggregate dispersion, 200 ml ultra-pure water was added to each sample and treated twice with 5 min shaking (shaking plate 3015, GFL Gesellschaft Für Labortechnik mbH, Germany) and 5 min ultrasonic at 480 W, resulting in an energy density of 720 J ml^{-1} (SONOREX RK 102 H, 35 kHz, 480 W, Bandelin, Germany).

(ii) **Density separation**: For density separation at $\rho = 1$ g cm^{-3}, another 200 ml of ultrapure water was added and centrifuged (6–16 S, Sigma Laborzentrifugen GmbH, Germany) at 2800 rpm for 30 min (Figure SI3B).

(iii) **Freezing and Filtration**: For freezing and filtration, 50 ml of ultrapure water was carefully added, an aluminium foil cylinder was placed on the top of the centrifugation tube (to 'guide' the ice during freezing), and the sample was then frozen at -18 °C for a minimum of 8 h (Fig. SI3C). The ice cap containing the low-density fraction ($\rho < 1$ g cm^{-3}) was removed by rinsing the edge between the ice and the centrifuge tube with 96% ethanol (ethanol denatured with 1% methyl ethyl ketone) and finally splitting it with a spatula. To apply the sample to a 2.5 cm diameter, white, phosphate-free, cellulose round-filter with a pore size of 4 µm (5.5 cm, 169 G, Macherey-Nagel, Germany), the ice cap was melted in a glass funnel and passed a filtration vessel (30 ml glass filter funnel head with blue PP funnel and two Flour-Caoutchouc seals, EAN: 4032051032088, DURAN, Schott AG, Germany) (Fig. SI3D). Once dried, the cellulose filter was carefully removed with a spatula and placed into a glass petri dish for subsequent analysis using the 3D LSCM.

3D Laser Scanning Confocal Microscopy measurement

The sample measurement was performed with a 3D LSCM, which combines a 404 nm semiconductor laser with a CMOS colour camera embedded in a depth-in-focus optical scanning system (Fig. 1B). For scanning the entire sample filter (ø 2.5 cm) while keeping a reasonable measurement time of 6 to 8 h, a medium magnification of 240x was used in the high-speed scanning mode and a height pitch of 4 µm (height resolution = 4 µm), with a coaxial light brightness and the laser brightness set to 2.5 and 9027, respectively. This setup enabled scanning one sample filter in four parts, achieving a pixel size of 2.72 µm x 2.72 µm. Finally, four sample filters (ø 2.5 cm), representing the extracted material from one 100 g MP-soil mixture, were automatically measured in a row in 24 to 32 h (Fig. 1B). The resulting data from each scan (~ 280 MB) was automatically saved in the proprietary VK4 file format from Keyence. Using the open-source tool vk4-python-driver (free available via GitHub [61]) height information, RGB values, and laser reflection with resolution of ~ 5000 x ~ 5000 pixels or respectively data points, were extracted and transformed into a height map (stored as CSV file, ~ 200 MB), a RGB image (stored as TIFF file, ~ 70 MB), and a laser reflection (intensity) image (stored as TIFF file, ~ 40 MB) (Fig. 1B). In addition to the height information, the laser reflection image represented an important data layer for particle discrimination. Transparent MPs exhibited low reflected laser intensity and therefore appeared as dark structures in the reflection image (Fig. 1B).

Machine-learning-based data analysis

A three-step random forest classifier workflow was implemented (Fig. 1C) to automatically distinguish MP particles from soil and background structures based on colour, laser reflection, and 3D surface-derived features. The labelled data set for training and testing was created based on a certain amount of the 103 test samples (Table SI1-SI3). For MP annotation in spiked soil samples MP_{spik} data was used for MP identification (SI2.5.2; Fig. SI5). The workflow progressively refines the classification results, from pixel-level segmentation (Pixel Classifier) to object-based segmentation (Object Classifier) and binary segmentation (Binary Object Classifier) between MP and soil particles. All random forest classifiers were trained and tested using identical hyperparameters (*n_estimators* = 10, *random_state* = 42, *class_weight* = "balanced_subsample"). The Pixel and Object Classifiers were operated within a One-vs-One framework to respect a multiclass classification. This three-step random forest classifier workflow enhances classification by combining semantic (pixel-based) information with object-level morphological, surface complexity and roughness features derived from 3D LSCM. A subsequent principal component analysis (PCA) was applied to correct for particle-assigned background noise (Fig. 1D).

For methodological consistency, adapted random forest classifiers were additionally applied to pure MP_{spik} on microscopy cover slips and MP blank samples (Fig. SI4). These classifiers were trained on dataset-specific annotations due to differing background characteristics (Section S2.5). To classify MP_{spik} only a Pixel Classifier was used (Table SI1). For MP blanks Pixel, Object and Binary Classifiers as well as PCA was applied (Table SI1-SI3).

(i) **Pixel-level classification (Pixel Classifier)**: Raw 3D LSCM data were denoised using a median filter applied to the laser reflection and RGB images. In addition, gradient, gradient magnitude, and sine of the gradient were derived from the 2D height

map (Table SI4). Five of the 103 test samples were partially annotated and used for classifier training and testing with a random split ratio of 70:30 (Table SI1). This step produced a semantic, pixel-based classification.

The pixel-level classes "Black MP" and "Transparent MP" were subsequently converted into instance-level objects (Fig. 1C). Morphological operations, including line closing, hole filling, and removal of small objects (< 4 connected pixels), were applied. Object-based features and coordinates were extracted from the laser reflection, RGB images, and the 2D height map, providing surface descriptors (Table 3). For surface roughness the parameters Mean Peak-to-Valley Height (Rz), Arithmetic Average Surface Roughness (Sa) and Root Mean Square Height (Sq) was used. For surface complexity fractal dimension via Box Counting Method, Specific Surface Area (SSA), Surface Area Ratio (SAR), and 3D Shape Index was used.

(ii) **Object-level classification (Object Classifier)**: The extracted object-based features were used to train a second random forest classifier (Tabel S4). Twelve of the 103 test samples (including the five used in the previous step) were partially annotated and used for classifier training and testing with a random split ratio of 60:40 (Tabel S2). This step provided an instance-level classification of individual particles.

(iii) **Binary classification (Binary Object Classifier)**: In the final step, only selected surface descriptors (Table SI4) were used to train a binary random forest classifier (class 1 = "MP", class 2 = "Soil"). Five samples out of the annotated dataset from the Object Classifier were used for the classifier training and testing, with a random split ratio of 60:40 (Table SI3).

(iv) **Principal component analysis background noise correction**: MP blanks were analysed following the same three-step random forest classifier workflow (Fig. 1C), with adapted training data and feature selection, to monitor MP background noise and correct (Fig. 1D) MP_{det}. MP blanks made out of transparent MPs were used to analyse black MP background noise signals, and MP blanks made out of black MPs were used to analyse transparent MP background noise signals. For the PCA, the features Area-filled, Rz, Sa, and fractal dimension (Table 3) were used and compared with the principal components of MP background noise from MP blanks with initially detected MP from the three-step random forest classifier workflow. A 90th -percentile threshold was applied to assign MP as background noise or as true MP_{det}. Finally, only MP_{det} with a minimum length > 10.88 µm (4 pixels) were considered to ensure reliable detection. Consequently, the smallest MP size class < 53 µm (Table 2) is reported as 11–53 µm in the results. Based on their spatial coordinates, the final MP objects were reassigned to their corresponding surface and size analyses.

Method evaluation

Method performance was evaluated using mass-to-particle count conversion, statistical recovery rate (RR), similarity analysis and MP alteration control based on 103 test samples (Sect. Test materials, Tables 1 and 2).

Mass-to-particle count conversion

MP_{spik} count was estimated via mass-to-particle count conversion (Table 4). MP_{spik} was classified from the

Table 3 Surface quantification with N = measurement points, z = height value, $N_B(\epsilon)$ = number of boxes with ϵ the box size, k = principal curvatures of the height

Surface quantification	Definition
$R_z = z_{max} - z_{min}$	Mean Peak-to-Valley Height (Rz): Average difference between the highest peaks and lowest valleys [62]
$Sa = \frac{1}{N}\sum_{i=1}^{N} \lvert z_i - \bar{z} \rvert$	Arithmetic Average Surface Roughness (Sa): Average height variation across the surface [62]
$Sq = \sqrt{\frac{1}{N}\sum_{i=1}^{N} (\lvert z_i - \bar{z} \rvert)^2}$	Root Mean Square height (Sq): Standard deviation of the surface and is more to outliers than Sa [62]
$FD = -\frac{\log N_B(\epsilon)}{\log 1/\epsilon}$	Fractal Dimension via Box Counting Method (FD): Quantifies the complexity of the surface [63]
$SSA = \frac{Surface\ Area}{Volume}$	Specific Surface Area (SSA): Geometric surface area to volume ratio in the dimension μm^{-1}
$SAR = \frac{Surface\ Area}{Area_{filled}}$	Surface Area Ratio (SAR): Geometric surface area to area ratio
$Shape\ Index = \frac{2}{\pi}\tan^{-1}\left(\frac{k_1+k_2}{k_1-k_2}\right)$	3D Shape Index: Measure local surface curvature with the 2D height map [64]

Table 4 The microplastic (MP) abundance is estimated from gravimetrically determined spiking mass and individual MP volume derived from 3D Laser Scanning Confocal Microscopy (3D LSCM)

Size class [µm]	Polymer	Mass [mg/25 g soil]	Estimated MP abundance per/25 g soil (median [range])
1000	PP-fibre	0.1	11 [7–19]
100–250	PP-T	0.05	25 [15–40]
	LDPE-T		27 [14–48]
	LDPE-B		22 [11–38]
53–100	PP-T	0.02	69 [42–127]
	LDPE-T		72 [35–154]
	LDPE-B		53 [34–97]
< 53	PP-T	0.1	304 [150–575]
	LDPE-T		412 [136–1071]
	LDPE-B		98 [57–265]

The range represents estimates calculated from the median, 75th, and 25th percentiles of the individual MP volume distribution (median [range]). Because MP number is inversely proportional to MP volume, smaller volumes yield higher MP numbers. The number of individually characterised MPs (N) and the underlying volume distributions used for the mass-to-particle conversion are provided in Table SI5. MP-type is defined in Table 2

background (cover slip) using a One-vs-One random forest Pixel Classifier (accuracy of 98.9%, Table SI1, Table SI4, Fig. SI6). The MP classified instance-level objects were manually differentiated according to individual MPs and conglomerates (Fig. SI2). Only individual MPs were included for volume quantification (Table SI5). Because MP volumes were non-normally distributed, median as well as 25th (P25), and 75th (P75) percentiles were used for MP number estimation (Sect. S2.6). As the MP number is inversely proportional to individual MP volume, smaller MP volumes (P25) yield higher estimated MP numbers, whereas larger volumes (P75) yield lower MP numbers.

Statistical recovery rate

RR was calculated as the ratio of MP_{det} to estimated MP_{spik}.

$$RR = \frac{MP_{det}}{MP_{spik}} \times 100\ [\%] \quad (1)$$

Because MP_{spik} was estimated as a range (P25-P75), detection results within this range were considered full recovery (RR = 100%). If MP_{det} fell outside this interval, RR was calculated using the corresponding boundary value:

- If $MP_{det} < MP_{spik}$ (P75):

$$RR = \frac{MP_{det}}{MP_{spik(P75)}} \times 100\ [\%] \quad (2)$$

- If $MP_{det} > MP_{spik}$ (P25):

$$RR = \frac{MP_{det}}{MP_{spik(P25)}} \times 100\ [\%] \quad (3)$$

Arithmetic mean RR and standard deviation were calculated from triplicate MP-soil spiked samples. For transparent PP-T, LDPE-T and PP fibres samples, only transparent MPs were evaluated. For LDPE-B samples only black MPs were evaluated.

Similarity analysis

MP_{det} is validated based on morphological similarity with MP_{spik}. To validate similarity a PCA was performed using size dependent and independent morphological features (area-filled, Rz, Sa, fractal dimension; Table 3). MP_{spik} was segmented from the background (cover slip) using a One-vs-One random forest Pixel Classifier and analysed on size and surface properties (accuracy of 98.9%, Table SI1, Table SI4, Fig. SI6). Based on Euclidean distances in the PCA space, silhouette coefficients [65] were calculated to quantify clustering. The silhouette coefficient ranges from −1 (incorrect clustering) to +1 (well-separated clusters). For interpretation, similarity levels were classified as: 0-0.25 strong similarity (no distinct clustering); 0.25–0.55 reasonable similarity; 0.55–0.75 weak similarity; and 0.75-1 no similarity (distinct cluster) [66].

Microplastic alteration control

To address potential alterations in MPs during extraction, the probability density of the dimensionless surface-complexity parameter, fractal dimension, was compared between MP_{spik} and MP_{det}. Probability density estimation was performed using a Gaussian kernel density estimator (Silverman's rule, bw_adjust = 1.0, 512 evaluation points). A comparison was conducted for MP_{det} in ultrapure water (MP blanks) and in soils S1, S2, and S3 to evaluate matrix-dependent extraction effects. In addition, black soil particles (representing SOM) and transparent mineral particles were analysed to distinguish matrix effects from true MP alteration.

Data processing and statistical analyses

Raw 3D LSCM data in VK4 format were first converted into 2D height maps using a Bash script executed in Windows PowerShell. Image annotation was performed in Fiji [67] using the open-source plugin LABKIT [68]. All subsequent data processing and analysis were performed using Python v3.12, compiled with the Spyder IDE 5.5.1 (Spyder, 2024) within Anaconda Navigator v2.6.5 [69]. The Python library scikit-learn v1.5.2 [70] was used for machine learning-based data analysis, PCA, and the silhouette score calculation. For image processing, the Python libraries scikit-image [71], SciPy v1.13.1 [72], and

the computer vision library OpenCV v4.10.0 were used. The function measure.regionprops from scikit-image was applied for object-based size analysis and feature extraction, while the function Delaunay from SciPy was used for volume calculations. Mathematical operations on object-based height values were performed using NumPy v1.26.4 [73] to quantify surface parameters as defined in Table 3 and to compute statistical measures, including mean, standard deviation, median, percentiles and Gaussian kernel density estimator. Data organisation was managed using pandas v2.2.2 [74]. All machine-learning analyses were performed on a laptop (Intel® Core™ i7-8565U CPU @ 1.80 GHz, 4 cores, 8 logical processors, 32 GB RAM). The computation of fractal dimension for the MP_{spik} dataset required increased computational resources due to the box-counting procedure applied across multiple scales. This step was therefore executed on a workstation equipped with a dedicated graphics processing unit and parallelised across 16 CPU cores. All subsequent analyses of spiked soil samples and blanks were performed on the laptop.

Results

Within three working days, four independent 25 g samples (< 2 mm soil; total 100 g) were processed in parallel using the developed workflow, which integrates MP extraction, automated 3D LSCM measurement, and machine-learning-based data analysis (Fig. 1A-D).

Detection performance and recovery

Machine learning performance and feature relevance

The multiclass pixel classifier achieved an overall accuracy of 98.2%, while the object classifier achieved an overall accuracy of 94.8%, and the binary classifier achieved an overall accuracy of 80.7% (Fig. SI6–SI8). The reduction in recall compared to the multiclass classifier reflects stricter discrimination. Visual inspection by experts confirmed that the number of false positives detected MPs decreased with each classifier application (Fig. 1C-D). Feature important was driven by surface, laser reflection and colour-related descriptors for the Pixel and Object Classifier. For the Pixel Classifier, the first three important features were the three colour channels red, green and blue. With the implementation of laser reflection and surface features, the classification could be refined. For the Object Classifier, the colour values were reduced to the red channel with the highest importance, followed by laser reflection, shape index, fractal dimension, SSA, SAR, Sq and Rz (Table SI4). The final Binary Classifier relied exclusively on surface-related descriptors: SAR, Sa, fractal dimension and Rz (from high to low importance), indicating that MP discrimination was based on structural characteristics rather than colour information. The application of the hierarchical classification workflow progressively reduced the number of false-positive MP detections in soil blanks, with PCA-based background noise correction and size threshold (Objects > 10.88 µm in minimum length) providing the final refinement step (Fig. 1C-D).

Recovery and similarity

Because background MP-like objects differed between soil matrices (Fig. 3), recovery results are presented for all soils (S1–S3); however, overall recovery calculations are additionally reported with and without S1 to account for matrix-dependent background interference.

(i) **Microplastics particles 100–250 µm and fibres 1000 µm**: For soils S2 and S3, statistical recovery rates of 100% were achieved for PP-T, LDPE-T, and LDPE-B (Fig. 2B). In the case of PP-fibres, 100% recovery was achieved in S3 (Fig. 2A), while S2 showed a slight overestimation (106.0% ± 6.6%). Silhouette coefficients indicated strong (LDPE-T in S2, LDPE-B in S2 and S3; Table 5) to reasonable similarity (Table SI6). In contrast, S1 showed 100% recovery only for PP-T. LDPE-T was slightly overestimated (109.0% ± 12.8%), while strong overestimations were observed for PP-fibres (164.9% ± 56.1%) and LDPE-B (396.8% ± 10.3%). Correspondingly, weak similarity was detected for PP-fibres in S1 (Table 5), whereas LDPE-T, PP-T, and LDPE-B showed reasonable similarity. MP blanks showed 100% recovery for LDPE-T (Fig. 2B). Overestimations were observed for PP-T (141.5%), LDPE-B (154.3%), and PP-fibre (211%; Fig. 2A). With a similarity between strong (Table 5) and reasonable (Table SI5). When S1 was excluded due to elevated background levels (see Fig. 3), reliable quantification of transparent, black, and weathered MPs (Table 2), was achieved for this size class, resulting a mean recovery of 104% ± 14.5%.

(ii) **Microplastic particles 53–100 µm**: In S2 and S3, the statistical recovery rates decreased. LDPE-T showed the highest recoveries (74.6% ± 23.8% in S2; 61.5% ± 10.8% in S3), followed by LDPE-B (64.2% ± 7.8% in S2; 41.2% ± 6.4% in S3) (Fig. 3C). PP-T presented the lowest recoveries (37.7% ± 5.1% in S2; 34.3% ± 16.1% in S3). Similarity remained within the range of strong (Table 2) to reasonable (Table SI6). For S1, statistical recovery rates were 97.6% ± 3.4% (PP-T), 93% ± 7.7% (LDPE-T), and 130.2% ± 27.4% (LDPE-B), with similarities between strong (Table 5) and reasonable (Table SI6). The MP blanks (Fig. 3C) showed 100% recovery for all MP-types. When S1 was excluded due to elevated background levels (see Fig. 3), reliable quantification of transparent, black, and

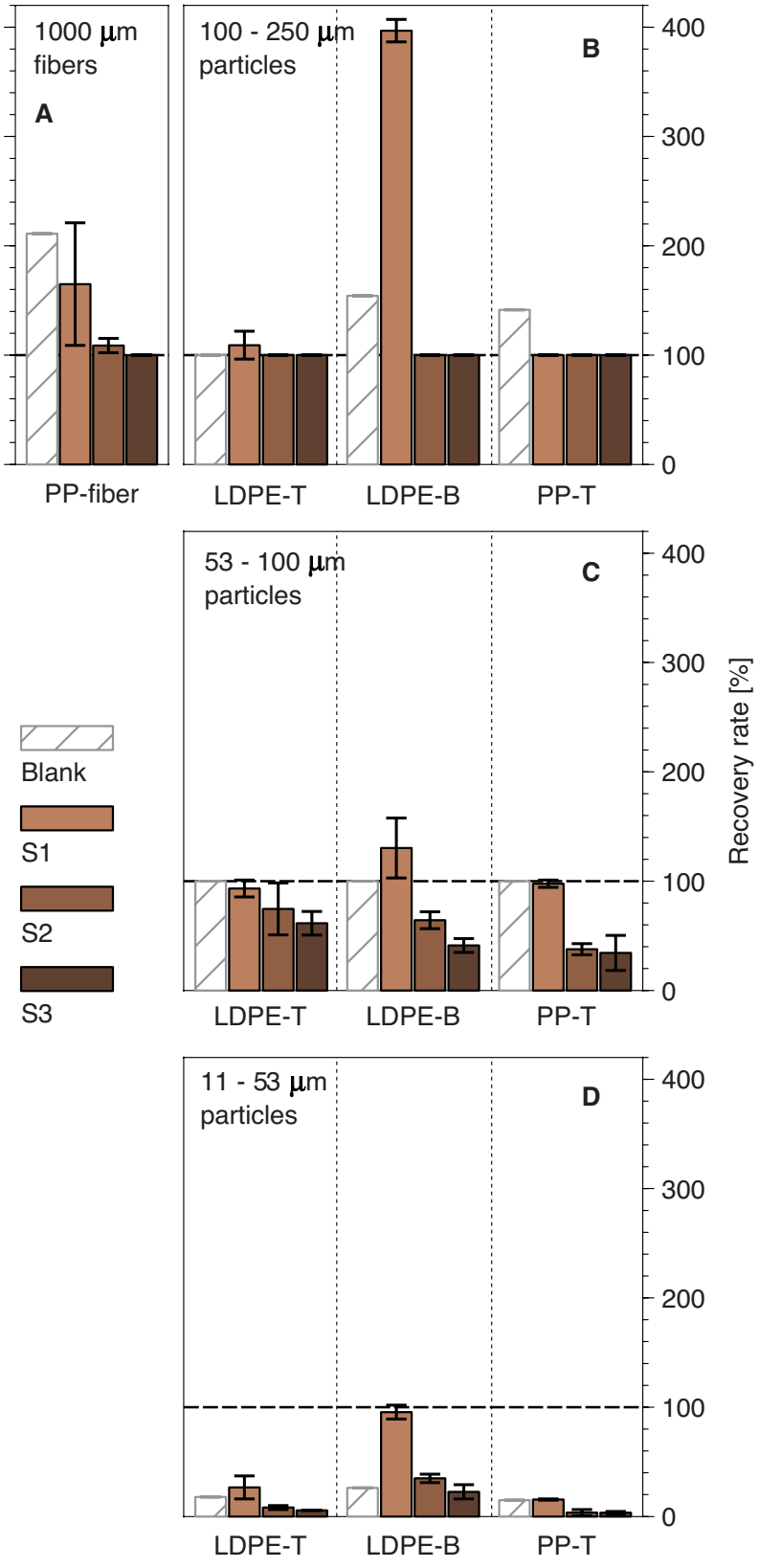

Fig. 2 Mean recovery rates inclusive standard deviation (error bars) for the three microplastic (MP) size classes (**A**-**D**), the three different soils (S1 to S3) and the MP blank. The recovery rate of 100% is indicated by a horizontal line. For the abbreviations of the different plastic particles and fibres, see Table 2

Table 5 Summary of strong (≤ 0.25) and weak (≥ 0.55) similarity cases identified by silhouette coefficient across MP size classes and soil matrices (mean ± standard deviation (SD))

MP size [µm]	MP type	Soil/MP blank	Similarity coefficient	Similarity class
1000	PP-fibre	S1	0.6 ± 0.1	Weak
	PP-fibre	S3	0.2 ± 0.1	Strong
100–250	PP-T	S3	0.2 ± 0.0	Strong
	LDPE-T	MP blank	0.1	Strong
	LDPE-T	S2	0.1 ± 0.0	Strong
	LDPE-B	S2	0.2 ± 0.1	Strong
	LDPE-B	S3	0.2 ± 0.1	Strong
53–100	LDPE-T	MP blank	0.2	Strong
	LDPE-T	S1	0.2 ± 0.1	Strong
	LDPE-B	MP blank	0.2 ± 0.0	Strong
11–53	PP-T	S3	0.6 ± 0.1	Weak
	LDPE-T	MP blank	0.1	Strong
	LDPE-B	S1	0.1 ± 0.1	Strong

MP blanks were created one per MP-type; therefore, no mean ± SD is available. All remaining combinations that showed reasonable similarity are provided in Table SI6. Soils defined in Table 1 MP type is defined in Table 2

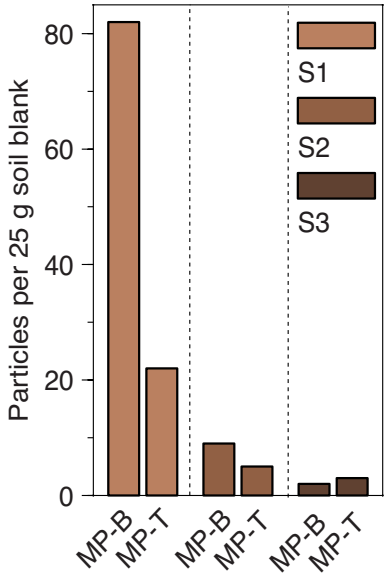

Fig. 3 Transparent and black microplastic (MP-T, MP-B) detected in the soil blanks of S1, S2 and S3

weathered MPs (Table 2), was achieved for this size class, resulting in a mean recovery of 59.1% ± 25.7%.

(iii) **Microplastics 11–53 µm**: For the smallest size class, recovery decreased substantially across all soils (Fig. 3D). Excluding S1, a mean recovery of 14.0% ± 12.4% was achieved. The highest recovery within the size class was observed for LDPE-B blank (26.2%), with a reasonable similarity (Table SI6). Reliable detection of MPs below 53 µm was therefore not achieved.

(iv) **Overall recovery**: Across all MP types (11–250 µm and fibres), varied between soil matrices. In particular, S1 showed strong overestimations, resulting in an overall mean recovery of 123.0% ± 104.0%, compared to 63.2% ± 39.5% for S2 and 56.9% ± 40.0% for S3. MP blanks alone achieved 96.6% ± 63.5%. Given the pronounced overestimation observed in S1, overall recovery was additionally evaluated, excluding this soil matrix. When S1 was excluded, the mean recovery across all MP types was 65.3% ± 45.0%. MP size-dependent effects were also evident. Excluding the smallest MP size fraction (11–53 µm), the overall mean recovery for transparent and black MPs ≥ 53 µm increased to 87.2% ± 34.7%. Under these conditions, S2 and S3 achieved 83.6% ± 26.5% and 76.7% ± 29.7%, respectively, while MP blanks reached 129.6% ± 42.6%. For transparent MPs increased from 59.8% ± 42.7% (MP ≥ 11 µm) to 81% ± 28.9% (MP ≥ 53 µm). Similarly, black MPs increased from 60.5% ± 31.9% (MP ≥ 11 µm) to 76.3% ± 26.6% (MP ≥ 53 µm). Across soils with low to medium POM content (S2 and S3), a mean recovery of 80% ± 28% was achieved for transparent and black MPs ≥ 53 µm.

(v) **Initial MP soil background contamination**: Soil blanks revealed matrix-dependent background contamination prior to MP_{spik} (Fig. 3). In S1, 82 black and transparent 22 MP-like objects were detected. In contrast, S2 and S3 showed substantially lower background levels with 14 and 5 detected objects, respectively. The elevated background signal in S1 corresponds to the strong recovery overestimations and explains the matrix-dependent variability observed in the recovery assessment.

Microplastic alteration

To evaluate potential surface alteration during extraction, fractal dimension was analysed for MPs in the 100–250 µm size class for MP_{spik} and MP_{det}. Fractal dimension serves as a dimensionless descriptor of surface complexity, with higher values indicating greater structural irregularity (higher complexity). The analysed MPs comprise virgin LDPE-T (Fig. 4A) and LDPE-B (Fig. 4B) materials and weathered PP-T (Fig. 4C; Table 2). Fractal dimension distributions were compared between MP_{spik} and MP_{det} in MP blanks, S1, S2, and S3, and with detected soil-associated particles (Fig. 4D). Across all MP types and sample matrices, fractal dimension increased after the MP extraction procedure relative to MP_{spik}.

For virgin LDPE-T, the lowest deviation from the MP_{spik} distribution was observed in the MP blank (Fig. 4A). Virgin LDPE-T in soils S1, S2, and S3 fractal

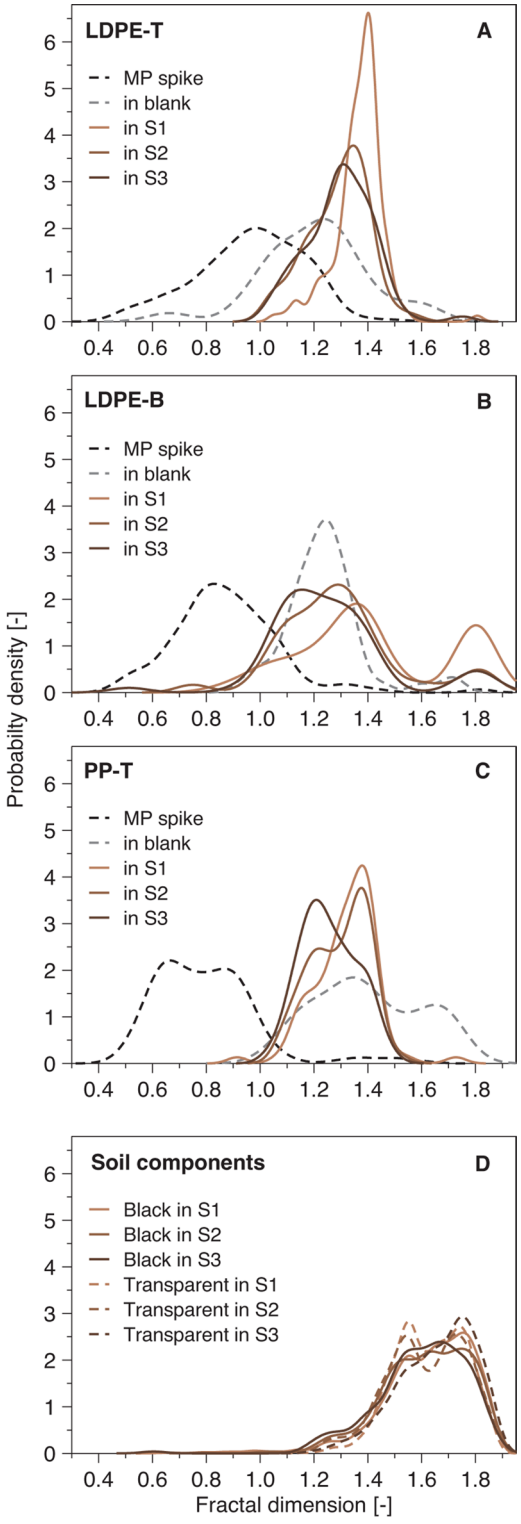

Fig. 4 Probability density distribution of the fractal dimension for the microplastic (MP) size 100–250 µm before spiking, and after measurement in the MP blank and in soils S1, S2, and S3 (**A**-**C**). (**D**) is fractal dimension of soils (S1 to S3) without plastics. The fractal dimension of the pure soil measurements was done separately for transparent (e.g. silicates) and black (e.g. organic carbon) soil components. For the abbreviations of the different plastic particles, see Table 2

dimension distributions partially overlap with MP_{spik}, but with a different curve profile. For virgin LDPE-B, fractal dimension in MP blanks and in all soils showed a distinct shift towards increasing fractal dimension, with LDPE-B in S1 showing a bimodal distribution (Fig. 4B). For weathered PP-T, fractal dimension distributions in the MP blank showed a distinct shift compared to MP_{spik} (Fig. 4C). The fractal dimension distributions of weathered PP-T detected in soil samples were more comparable to those of the soil-associated particles detected (Fig. 4D). Overall, the extraction procedure resulted in measurable changes in fractal dimension distributions across MP-types and matrices.

Discussion

Method performance

Robust detection across soil matrices and microplastic sizes

Robust MP detection was achieved in agricultural soils with low to medium POM content (S2 and S3), particularly for MPs ≥ 53 µm (Fig. 3A-C). In S2 and S3, transparent and black MPs ≥ 53 µm were reliably detected with strong to reasonable similarity and consistent recovery rates, demonstrating that the presence of SOM does not inherently prevent automated MP quantification. In contrast, performance decreased in the high-POM soil (S1), where structural similarity between POM and black LDPE-B or PP-fibres led to increased false-positive assignments. Expert inspection of S1 soil blanks confirmed that the majority of initially detected black MPs represented misclassified POM structures rather than true MPs. The elevated abundance of transparent MPs in S1 soil blanks could be traced back to contamination from the white/transparent polypropylene sample bag. The workflow was intentionally designed without oxidative or corrosive SOM removal. Consequently, POM structures remained physically intact and available for classification, increasing the likelihood of morphological overlap. These findings demonstrate that the developed workflow does not eliminate matrix interference but operates within defined matrix constraints. Detection robustness, therefore, declines with increasing POM content and particle complexity, consistent with H2. The MP size further influenced performance. Reliable quantification was achieved for MPs ≥ 53 µm, whereas recoveries declined substantially for MPs 11–53 µm (Fig. 3D). Reduced performance for MPs 11–53 µm was primarily associated with the PCA-based background noise correction, in which MPs 11–53 showed feature similarity (filled area, Rz, Sa, and fractal dimension) with background noise, leading to partial misclassification. The misclassification was clearly observed in the MP blank of LDPE-B 11–53 µm. This limitation is not introduced by the random forest workflow or by the selected 3D LSCM magnification. Overall, H2 is supported: robust MP

detection is achievable in agricultural soils despite not removing SOM, but performance decreased with high POM content and for MPs below 53 µm.

Morphology and surface-based discrimination

The 3-step random forest classification workflow combined colour, laser reflection at pixel level, with size-independent morphological and surface descriptors at object level (Table SI4). Notably, only surface descriptors were retained for the final binary classification. Colour and laser reflection improved initial separation between transparent and black MPs and background structures. This was particularly evident in S1, where transparent MPs were less affected by false-positive assignments than black MPs due to the inclusion of colour and laser-reflection features in the Pixel Classifier. At the object level, discrimination relied primarily on morphological and surface descriptors, including surface complexity and roughness parameters. Feature importance analysis confirmed the contribution of these descriptors to classification performance. Importantly, object-based classification was designed to operate independently of particle size. No watershed segmentation was applied, thereby avoiding size-dependent particle splitting and potential artefacts associated with irregular particle geometries [37]. The size-independent instance segmentation allowed attached MPs to be detected as single objects. However, fibrous MPs and MPs with thin extensions were occasionally detected as multiple fragments. A reliable watershed-based separation was not feasible due to the irregular shapes of fragments and the risk of artificial over-segmentation. The chosen parameter set in the instance segmentation step, therefore, prioritised size-independent segmentation over aggressive particle splitting (Fig. 1C). Reduced recovery for MP 53–100 µm in S2 and S3 may reflect stronger particle–matrix interactions in loam- and clay-rich soils. The weathered surface morphology of PP-T 53–100 µm may further enhance adhesion to soil particles, complicating morphology-based discrimination under matrix attachment conditions. Overall, H3 is largely supported: MPs can be distinguished from soil particles primarily through size-independent morphological and surface descriptors, while colour features and laser reflection enhance robustness in complex matrices. Performance remains influenced by matrix heterogeneity and particle–matrix interactions.

Microplastic surface alteration during extraction

Fractal dimension analysis revealed a systematic increase in surface complexity after extraction across all MP types (virgin and weathered), indicating moderate surface alteration during the extraction procedure (Fig. 4A-C). The bimodal fractal-dimension distribution observed for LDPE-B in S1 indicates the presence of two structurally distinct object populations. This pattern may reflect a combination of true LDPE-B particles and structurally similar matrix-derived objects or fragmented particles generated during extraction (Fig. 4C-D). The extraction workflow involved mechanical shaking, ultrasonication (720 J ml^{-1}), centrifugation, freezing, and filtration with a vacuum pump. Among these, ultrasonication likely contributed most strongly to increased surface complexity and partial fragmentation. Ultrasonic energies above 60 J ml^{-1} are known to disturb POM [75]; however, their effects on MP surfaces remain insufficiently quantified [46]. Mechanical shaking and centrifugation may additionally promote particle–particle and particle–matrix abrasion, while freezing and thawing cycles can introduce physical stress. The observed increase in fractal dimension suggests that these combined mechanical treatments may induce moderate surface alteration. In addition, apparent increases in surface complexity may also result from the attachment of soil-derived particles (e.g., SOM or silicates) to MP surfaces. Such coating effects can artificially increase the fractal dimension without reflecting intrinsic surface alteration. However, similar increases observed in MP blanks indicate that mechanical treatment alone accounts for the observed changes, suggesting that both surface modification and particle attachment may influence the results. Surface property is a key parameter in ecotoxicological assessment, as increased surface complexity may influence sorption behaviour, and interactions with soil invertebrates [30, 34, 76]. Therefore, preservation of surface properties is relevant not only for analytical detection but also for environmental interpretation. Despite the measurable increase in fractal dimension, particle morphology remained sufficiently preserved to allow reliable classification and quantification of MPs ≥ 53 µm. Compared to workflows that rely on oxidation or density separation using corrosive substances, the present extraction strategy avoids chemical alteration but may induce moderate mechanical modification. Thus, H1 is only partially supported: while the extraction procedure enabled reliable detection, it also caused measurable changes in surface complexity. Optimising dispersion energy and mechanical stress may further reduce alteration in future applications. To position the developed workflow within the current methodological landscape of MP detection in soils, recovery performance and detection limits are compared with established analytical approaches in the following section.

Method evaluation and validation

A review found that only 35% of the published MP studies performed recovery tests based on controlled spiking experiments [44]. Direct comparison of recovery rates across studies remains challenging due to differences in

MP size, colour, polymer type, soil matrix and spiking concentration. Therefore, comparison was restricted to studies using comparable MP materials.

Fluorescence microscopy achieved mean recoveries of 82% ± 15% for white LDPE (20–150 µm) in sandy soil and 88% ± 7% in a loamy soil [37], comparable to transparent MPs (53–250 µm) in S2 and S3 in the presented study. However, for black PBAT/PLA (100–250 µm) recoveries decreased to 17% ± 7% in sandy soil and 45 ± 20% in loamy soil [37]. Similarly focal plane array (FPA)-µ-FTIR achieved 57% ± 13% for transparent LDPE (10–150 µm) in a sandy soil and 29% ± 0% in a loamy soil, while black PBAT/PLA (10–250 µm) achieved 50% ± 2% in loamy soil and 49% ± 16% in sandy soil [40]. Stereomicroscopy, in combination with machine learning, reported higher recoveries for black tyre wear particles (> 35 µm), reaching 85% ± 10% [3]. Stereomicroscopy, in combination with a heat plate, achieves recoveries > 80% for white LDPE < 150 µm and PP < 400 µm [38]. Compared with fluorescence microscopy and FPA-µ-FTIR, the 3D LSCM workflow developed here achieved higher mean recoveries for black MPs in the 53–250 µm size range. Whereby stereomicroscopy in combination with machine learning achieved higher recoveries for black tyre wear than the 3D LSCM workflow. However, the applied extraction procedure was specifically designed for light-density polymers (LDPE, PP) and is not suitable for high-density polymers such as PBAT/PLA or tyre wear particles. For LDPE-T (53–250 µm), fluorescence microscopy [37] and FPA-µ-FTIR [40] yielded recoveries comparable to those of the 3D LSCM workflow.

While differences in recovery between methods are partly attributable to MP size and polymer, colour and matrix composition emerge as additional critical factors influencing detection performance. Matrix interference caused by SOM represents a common limitation across MP detection workflows [40, 43]. Many established approaches, therefore, include oxidative SOM removal prior to detection [44]. While such purification steps improve recovery, they may alter MP [49, 50] and increase processing time. In the present study, no oxidative and corrosive purification was applied. Therefore, the observed false-positive assignments in high-POM soil (S1) reflect the physical coexistence of POM and MPs, which was caused by the intended gentle sample purification rather than a methodological classification issue. Optical differentiation between dark MPs and organic matter is particularly challenging. Similar colour-dependent limitations are reported for microscopic and microspectroscopic approaches. In fluorescence microscopy, Nile Red staining may yield a low signal-to-noise ratio for black MPs [37]. In µ-FTIR analysis, dark or opaque particles can block the infrared beam [45], and particle thickness may further affect spectral quality [43]. Polymer additives, such as fillers, pigments, and dyes, in black polymers may interfere with µ-Raman measurements [47]. These colour-dependent limitations likely contribute to the reduced recovery rates reported for dark MPs in spectroscopic approaches. These findings indicate that interference from SOM and colour-dependent detection challenges are not unique to the present workflow but represent a general limitation in MP analysis. The current approach demonstrates that reliable quantification of black LDPE is achievable in the presence of low to medium POM content without oxidative or corrosive purification. High POM matrices define the operational limit of this workflow.

An additional distinction concerns spiking concentrations. Previous studies often applied substantially higher concentrations (e.g., 300 mg kg^{-1} [37, 40]) than those used here. In the present study, spiking concentrations were selected to reflect environmentally realistic levels, consistent with the reported global MP concentration up to 13,000 items kg^{-1} (4.5 mg kg^{-1}) [77]. Further, a review study from 2024 estimated a global mean of 2900 ± 7600 MP items kg^{-1} in agricultural soils with sludge amendments 3700 ± 8800 MP items kg^{-1} [78]. Validation under realistic concentration levels increases ecological relevance but may reduce apparent recovery rates compared to high-concentration laboratory tests.

The recovery calculation was based on a statistical mass-to-particle-count conversion approach. Counting the spiking material by particle-by-particle was not feasible due to MP overlay in 3D LSCM images (Fig. SI2), particularly for size classes < 100 µm. Volume quantification of the spiking material was performed on a flat background (microscopy cover slip) to derive a statistical estimate of individual MP particles. The estimation is based on the volume distribution of a representative number of MPs characterised as individual particles per polymer type and size class (Tab. SI5). Natural variability in particle size and shape introduces uncertainty into particle number estimates, particularly for smaller size classes. In addition, non-spherical particle geometries, such as fibrous MPs, may deviate from idealised size classification and sieving behaviour, potentially introducing further uncertainty in the mass-to-particle count conversion. Similar methodological challenges have been reported in other studies. Empirical models to estimate particle numbers were used, based on the assumption of spherical particles [38], shape-dependent volume estimations [79, 80] or particle counters [37].

Reliable size detection limits detection represents another critical validation parameter. The developed workflow enables reliable quantification down to 53 µm. MPs down to 11 µm were detectable but not reliable quantifiable due to low recoveries. In comparison µ-FTIR reports reliable limits around 100 µm using µ-FTIR [80],

while possible detection limits down to 10 µm have been described [41]. Microscopy-based approaches reports reliable down to 63 µm with video microscopy [20], 49 µm [81], 30 µm [82], and 35 µm [3] with Stereomicroscopy, and 20 µm with fluorescence microscopy [37]. Thus, the achieved reliable quantification limit of 53 µm places the method within the competitive range of advanced microscopy-based approaches.

Direct laboratory cross-validation with established spectroscopic methods is constrained by methodological differences. Spectroscopic approaches such as µ-FTIR and µ-Raman typically require extensive SOM purification to obtain reliable spectra [40, 41]. The present extraction strategy intentionally avoided oxidative digestion to preserve surface morphology and minimise chemical alteration, thereby limiting direct compatibility with spectroscopy-based validation. The inclusion of black LDPE further complicates µ-FTIR and µ-Raman validation [43, 45, 47]. ATR-FTIR was not applicable due to the small MP size (< 500 µm) [3, 41, 43], and while Pyr-GC-MS could confirm total polymer mass, it would not provide particle-resolved validation [35]. Instead, validation was performed by morphological comparison of detected MPs with the original spiking material. A similarity analysis based on PCA incorporated surface and morphological descriptors, including a size-related parameter. Colour information was excluded because MPs detected in soil partially adopted soil-associated optical characteristics and were therefore not directly comparable to spiking material.

The similarity assessment showed predominantly reasonable similarity across MP–soil spiking combinations, with only two cases presenting weak similarity (Table 5) and none showing absence of similarity. This supports that the detected objects correspond structurally to the intended spiking material. While morphological similarity cannot replace chemical identity confirmation, it provides robust particle-level validation within the non-destructive workflow. Future applications may integrate selective spectroscopic confirmation on representative subsamples.

The extraction workflow relies on mechanical dispersion (shaking, ultrasonication at 720 J ml^{-1}, centrifugation, freezing) and density separation using ultra-pure water. Ultrasonic energies above 60 J ml^{-1} are known to disturb POM [75], and although the same or higher energy densities have been reported in other studies (720 J ml^{-1} [83]; 21600 J ml^{-1} [81]; 105600 J ml^{-1} [84]), the effects on MP surface properties remain insufficiently quantified [46]. Alternative approaches include freeze-drying for gentle but more time-intensive (24 h) dispersion [41] or chemical oxidation to remove SOM [15, 37, 40]. However, oxidative treatments may reduce recovery rates for light-density MPs [20] and can induce chemical or thermal alteration [49]. Zinc chloride density separation is widely used [20, 37, 41, 80], but may cause corrosion of polymer surfaces [40, 44]. Instead of using zinc chloride for density separation, non-corrosive high-density salt solutions could be used, such as sodium chloride [54], calcium chloride [54], sodium bromide [3, 85], and sodium iodide [86], or ultra-pure water [38, 81, 87]. This study focused on light-density MP polymers (PP and LDPE), and using ultra-pure water, the present workflow avoids oxidative and corrosive reagents while enabling hazard-free extraction. However, it remains limited to light-density polymers and may induce moderate mechanical surface modification, as indicated by increased fractal dimension.

Overall, the developed workflow provides hazard-free extraction, colour-explicit validation, and automated morphological analysis under environmentally realistic conditions, while achieving competitive recovery performance for transparent and black light-density MPs in agricultural soils.

Complement existing methods

The developed 3D LSCM workflow complements established spectroscopic approaches by adding quantitative surface and morphological characterisation at the particle level. While techniques such as ATR-FTIR, µ-FTIR, µ-Raman provide polymer identification at the particle level, they do not deliver systematic quantitative surface descriptors. Although specific µ-Raman is principally capable of three-dimensional mapping [45], its application to soil matrices remains limited and has not yet been systematically used for quantitative surface characterisation of MPs in soils. The presented workflow enables automated extraction of surface roughness (Sa, Sq, Rz), and surface complexity (fractal dimension, SSA, SAR) parameters directly from 3D height data. Surface morphology is recognised as relevant for environmental interactions and ecotoxicological effects [34, 76, 77]. Although SEM is frequently used for qualitative surface imaging of MPs, quantitative surface metrics are rarely extracted. The morphological parameterisation implemented here provides a reproducible and structured approach to surface quantification that could be complemented by SEM-based validation in future studies. The current workflow was trained explicitly for transparent and black MPs. Extension to additional MP colours would require expansion of the labelled training dataset. Increasing annotation diversity would improve generalisability across heterogeneous soil matrices. Furthermore, implementing advanced segmentation architectures, such as U-Net-based deep learning approaches, may enhance pixel-level discrimination in complex matrices and further improve the detection of small or weathered particles.

The extraction procedure was optimised for light-density polymers such as LDPE and PP, using ultra-pure water to avoid oxidative or corrosive substances and to preserve surface integrity. Adaptation to higher-density polymers (e.g., PET, PVC, tyre wear particles) would require modification of the density separation step. While heavy-salt solutions can enable separation of denser polymers, they may also extract larger fractions of SOM, particularly in soils with high POM content, thereby increasing matrix complexity and potentially requiring additional purification steps. Pretests revealed limitations when combining saturated sodium chloride or calcium chloride solutions with the freezing step required for clean phase separation after centrifugation [88–90]. At − 24.25 °C, saturated sodium chloride crystallised and formed hydrohalite ice mixtures [91] that interfered with separation and automated detection, whereas saturated calcium chloride did not freeze under these conditions. These physicochemical constraints must be considered when adapting the workflow to heavier polymers. In addition, the cellulose filter is not perfectly planar, which may influence the volume estimation of MP_{det} due to local surface waviness. Adaptation to flatter or spectroscopically compatible filter materials would improve volume quantification and further facilitate sequential morphological and chemical validation within a unified analytical pipeline. Overall, the developed workflow complements existing analytical methods by combining hazard and corrosive-reduced extraction, colour-explicit detection, automated morphological analysis, and quantitative surface characterisation under environmentally realistic conditions. Its integration into multi-method analytical strategies may enhance both robustness and informational depth in MP assessment of agricultural soils.

Conclusion

The developed workflow enables automated detection of transparent and black light-density MPs (LDPE and PP) in agricultural soils and fulfils the core objectives defined in this study. Using a corrosion- and oxidation-free extraction procedure combined with 3D LSCM, a three-step random forest classification, and PCA background noise correction, reliable detection was achieved for MPs ≥ 53 µm, which represents the current size limit for reliable quantification. For MP particles in the size range 53–250 µm and fibres (~ 1000 µm length), a mean recovery of 80% ± 28% was obtained in the sandy (S2) and silty (S3) soils with low to medium POM content. Performance decreased in the soil with high POM content and for smaller MP sizes, confirming that detection robustness declines with increasing matrix complexity and decreasing MP sizes, consistent with H2. Detection of MPs down to 10.88 µm (4 pixels; minimal length) was technically feasible. However, recoveries for MPs 11–53 µm were not sufficient for reliable quantification. Across all matrices, fractal dimension increased after extraction compared to the spiking material, suggesting moderate surface alteration. While the individual contributions of shaking, ultrasonication, centrifugation, and freezing cannot be isolated in the present workflow, MP morphology remained sufficiently preserved to enable classification and surface quantification ≥ 53 µm. Hypothesis H1 is therefore only partially supported, as morphological preservation depends on dispersion and separation conditions. A central advancement of the workflow lies in the quantitative integrations of 3D morphological descriptors. The method enables automated data analysis of MP size, 3D shape, volume, surface roughness (Peak-to-Valley Height (Rz), Arithmetic Average Surface Roughness (Sa) and Root Mean Square Height (Sq)) and surface complexity (fractal dimension, specific surface area, surface area ratio). Surface properties substantially enhanced MP discrimination from soil organic and mineral particles, supporting H3 and demonstrating that size-independent morphological and surface descriptors form the primary basis of classification. Colour information improved pixel-level discrimination, particularly for transparent MPs. The developed workflow allows processing of 100 g (soil < 2 mm) samples in approximately three days without extensive SOM purification or hazardous substances. By combining oxidative and corrosive free extraction, automated classification, and particle resolved 3D surface quantification under environmentally realistic spiking concentrations, the method provides a time-efficient and cost-conscious alternative to workflows requiring chemical oxidation and (semi-)manual particle analysis. Although currently limited to light-density polymers due to the applied density separation and limited to high POM contents under oxidative-free sample preparation, the developed workflow represents a significant step towards surface-property-resolved, automated MP assessment in agricultural soils. Reliable quantification (MPs ≥ 53 µm) was achieved in soils with low to medium POM without oxidative or corrosive purification. Integration with complementary spectroscopic or thermoanalytical techniques may further enhance polymer specificity while preserving the added value of quantitative particle-level surface characterisation.

Supplementary Information

The online version contains supplementary material available at https://doi.org/10.1186/s43591-026-00202-8.

Supplementary Material 1

Acknowledgements
We would like to acknowledge the members of the Water and Soil Resource Research group at the University of Augsburg, especially Luisa Wanger and Simon Scherer. Additionally, gratitude is extended to Bernhard Leitner and Jakob Faustmann from the Fraunhofer IGCV for providing polypropylene microplastic particles. We further thank the Bavarian State Environmental Agency (LfU), Germany, for providing soil property data for soils S2 and S3.

Author contributions
TS: Conceptualisation, methodology, machine learning, data processing, investigation, quality control, writing – original draft, visualisation; PF: Resources, writing review and editing, funding acquisition and supervision.

Funding
Open Access funding enabled and organized by Projekt DEAL. This work was supported by the Federal Ministry of Education and Research as part of the initiative Plastics in the Environment (grant no. 02WPL1447A-G).

Data availability
The datasets used and/or analysed during the current study are available from the corresponding author on reasonable request.

Declarations

Ethics approval and consent to participate
Not applicable.

Consent for publication
All authors approve the manuscript and give their consent for submission and publication.

Competing interests
The authors declare no competing interests.

Author details
[1]Water and Soil Resources Research, Institute of Geography, University of Augsburg, Alter Postweg 118, 86159 Augsburg, Germany

Received: 16 December 2025 / Accepted: 10 May 2026
Published online: 17 June 2026

References

1. Hurley RR, Nizzetto L. Fate and occurrence of micro(nano)plastics in soils: knowledge gaps and possible risks. Curr Opin Environ Sci Health. 2018;1:6–11. https://doi.org/10.1016/j.coesh.2017.10.006.
2. Frias JPGL, Nash R. Microplastics: finding a consensus on the definition. Mar Pollut Bull. 2019;138. https://doi.org/10.1016/j.marpolbul.2018.11.022.
3. Foetisch A, Grunder A, Kuster B, Stalder T, Bigalke M. All black: a microplastic extraction combined with colour-based analysis allows identification and characterisation of tire wear particles (TWP) in soils. Microplastics Nanoplastics. 2024;4. https://doi.org/10.1186/s43591-024-00102-9.
4. Müller A, Kocher B, Altmann K, Braun U. Determination of tire wear markers in soil samples and their distribution in a roadside soil. Chemosphere. 2022;294:133653. https://doi.org/10.1016/j.chemosphere.2022.133653.
5. Yukioka S, Tanaka S, Nabetani Y, Suzuki Y, Ushijima T, Fujii S, et al. Occurrence and characteristics of microplastics in surface road dust in Kusatsu (Japan), Da Nang (Vietnam), and Kathmandu (Nepal). Environ Pollut. 2020;256. https://doi.org/10.1016/j.envpol.2019.113447.
6. Paruta P, Pucino M, Boucher J. Plastic paints the environment. Environmental Action. 2022.
7. Turner A, Bridgwater A, Marshall E. Environmental transport and sorting of glass retroreflective microbeads and their potential as proxies for road marking paints. Sci Total Environ. 2024;954:176057. https://doi.org/10.1016/j.scitotenv.2024.176057.
8. Jambeck JR, Geyer R, Wilcox C, Siegler TR, Perryman M, Andrady A, et al. Plastic waste inputs from land into the ocean. Sci Am Association Advancement Sci. 2015;347:768–71. https://doi.org/10.1126/science.1260352.
9. Li S, Ding F, Flury M, Wang Z, Xu L, Li S, et al. Macro- and microplastic accumulation in soil after 32 years of plastic film mulching. Environ Pollut. 2022;300:118945. https://doi.org/10.1016/j.envpol.2022.118945.
10. Singh S, Chakma S, Alawa B, Kalyanasundaram M, Diwan V. Assessment of microplastic pollution in agricultural soil of Bhopal, Central India. J Mater Cycles Waste Manag. 2024;26:708–22. https://doi.org/10.1007/s10163-023-01805-6.
11. Dris R, Gasperi J, Rocher V, Saad M, Renault N, Tassin B. Microplastic contamination in an urban area: a case study in greater paris. Environ Chem CSIRO Publishing. 2015;12:592–9. https://doi.org/10.1071/en14167.
12. Huerta Lwanga E, van Roshum I, Munhoz DR, Meng K, Rezaei M, Goossens D, et al. Microplastic appraisal of soil, water, ditch sediment and airborne dust: the case of agricultural systems. Environ Pollut. 2023;316:120513. https://doi.org/10.1016/j.envpol.2022.120513.
13. Weber CJ, Bigalke M. Forest soils accumulate microplastics through atmospheric deposition. Commun Earth Environ Nat Publishing Group. 2025;6:702. https://doi.org/10.1038/s43247-025-02712-4.
14. Liu EK, He WQ, Yan CR. white revolution' to 'white pollution'—agricultural plastic film mulch in china. Environ Res Lett. 2014;9:091001. https://doi.org/10.1088/1748-9326/9/9/091001.
15. Piehl S, Leibner A, Löder MGJ, Dris R, Bogner C, Laforsch C. Identification and quantification of macro- and microplastics on an agricultural farmland. Sci Rep. 2018;8:17950. https://doi.org/10.1038/s41598-018-36172-y.
16. Steinmetz Z, Wollmann C, Schaefer M, Buchmann C, David J, Tröger J, et al. Plastic mulching in agriculture. Trading short-term agronomic benefits for long-term soil degradation? Sci Total Environ. 2016;550:690–705. https://doi.org/10.1016/j.scitotenv.2016.01.153.
17. Fabrizi A, Fiener P, Jagdhuber T, Van Oost K, Wilken F. Plasticulture detection at the country scale by combining multispectral and SAR satellite data. Sci Rep Nat Publishing Group. 2025;15:11339. https://doi.org/10.1038/s41598-025-93658-2.
18. FAO. Assessment of agricultural plastics and their sustainability: a call for action. 2021; https://doi.org/10.4060/cb7856en
19. Hofmann T, Ghoshal S, Tufenkji N, Adamowski JF, Bayen S, Chen Q, et al. Plastics can be used more sustainably in agriculture. Commun Earth Environ Nat Publishing Group. 2023;4. https://doi.org/10.1038/s43247-023-00982-4.
20. Braun M, Mail M, Krupp AE, Amelung W. Microplastic contamination of soil: are input pathways by compost overridden by littering? Sci Total Environ. 2023;855:158889. https://doi.org/10.1016/j.scitotenv.2022.158889.
21. Groß M, Mail M, Wrigley O, Debastiani R, Scherer T, Amelung W, et al. Plastic fruit stickers in industrial compostingsurface and structural alterations revealed by electron microscopy and computed tomography. Environ Sci Technol. 2024;58:7124–32. https://doi.org/10.1021/acs.est.3c08734.
22. Weber CJ, Santowski A, Chifflard P. Investigating the dispersal of macro- and microplastics on agricultural fields 30 years after sewage sludge application. Sci Rep. 2022;12:6401. https://doi.org/10.1038/s41598-022-10294-w.
23. Corradini F, Meza P, Eguiluz R, Casado F, Huerta-Lwanga E, Geissen V. Evidence of microplastic accumulation in agricultural soils from sewage sludge disposal. Sci Total Environ Elsevier. 2019;671:411–20.
24. Zhang S, Bao A, Lin X, Jia G, Zhang Q. Microplastic accumulation in agricultural soils with different mulching histories in xinjiang, China. Sustainability. 2023;15:5438. https://doi.org/10.3390/su15065438.
25. Boots B, Russell CW, Green DS. Effects of microplastics in soil ecosystems: above and below ground. Environ Sci Technol Am Chem Soc. 2019;53:11496–506. https://doi.org/10.1021/acs.est.9b03304.
26. de Souza Machado AA, Kloas W, Zarfl C, Hempel S, Rillig MC. Microplastics as an emerging threat to terrestrial ecosystems. Glob Change Biol Wiley Online Libr. 2018;24:1405–16. https://doi.org/10.1111/gcb.14020.
27. Huerta Lwanga E, Gertsen H, Gooren H, Peters P, van der Salánki T, et al. Microplastics in the terrestrial ecosystem: implications for lumbricus terrestris (oligochaeta, lumbricidae). Environ Sci Technol Am Chem Soc. 2016;50:2685–91. https://doi.org/10.1021/acs.est.5b05478.
28. Qi Y, Yang X, Pelaez AM, Huerta Lwanga E, Beriot N, Gertsen H, et al. Macro- and micro- plastics in soil-plant system: effects of plastic mulch film residues on wheat (triticum aestivum) growth. Sci Total Environ. 2018;645:1048–56. https://doi.org/10.1016/j.scitotenv.2018.07.229.
29. Qi Y, Ossowicki A, Yang X, Huerta Lwanga E, Dini-Andreote F, Geissen V, et al. Effects of plastic mulch film residues on wheat rhizosphere and soil properties. J Hazard Mater. 2020;387:121711. https://doi.org/10.1016/j.jhazmat.2019.121711.
30. Redondo-Hasselerharm PE, Rico A, Huerta Lwanga E, Van Gestel CAM, Koelmans AA. Source-specific probabilistic risk assessment of microplastics

in soils applying quality criteria and data alignment methods. J Hazard Mater. 2024;467:133732. https://doi.org/10.1016/j.jhazmat.2024.133732.
31. Katainen J, Paajanen M, Ahtola E, Pore V, Lahtinen J. Adhesion as an interplay between particle size and surface roughness. J Colloid Interface Sci. 2006;304:524–9. https://doi.org/10.1016/j.jcis.2006.09.015.
32. Jiang Y, Zhou S, Fei J, Qin Z, Yin X, Sun H, et al. Transport of different microplastics in porous media: effect of the adhesion of surfactants on microplastics. Water Res. 2022;215:118262. https://doi.org/10.1016/j.watres.2022.118262.
33. Rajupet S. DLVO interactions between particles and rough surfaces: an extended surface element integration method. Langmuir Am Chem Soc. 2021;37:13208–17. https://doi.org/10.1021/acs.langmuir.1c01492.
34. Liang Y, Luo Y, Shen C, Bradford SA. Micro- and nanoplastics retention in porous media exhibits different dependence on grain surface roughness and clay coating with particle size. Water Res. 2022;221:118717. https://doi.org/10.1016/j.watres.2022.118717.
35. Steinmetz Z, Kintzi A, Muñoz K, Schaumann GE. A simple method for the selective quantification of polyethylene, polypropylene, and polystyrene plastic debris in soil by pyrolysis-gas chromatography/mass spectrometry. J Anal Appl Pyrol. 2020;147:104803. https://doi.org/10.1016/j.jaap.2020.104803.
36. Eisentraut P, Dümichen E, Ruhl AS, Jekel M, Albrecht M, Gehde M, et al. Two birds with one stone—fast and simultaneous analysis of microplastics: microparticles derived from thermoplastics and tire wear. Environ Sci Technol Lett Am Chem Soc. 2018;5:608–13. https://doi.org/10.1021/acs.estlett.8b00446.
37. Le QNP, Halsall C, Peneva S, Wrigley O, Braun M, Amelung W, et al. Towards quality-assured measurements of microplastics in soil using fluorescence microscopy. Anal Bioanal Chem. 2025;417:2225–38. https://doi.org/10.1007/s00216-025-05810-6.
38. Zhang S, Yang X, Gertsen H, Peters P, Salánki T, Geissen V. A simple method for the extraction and identification of light density microplastics from soil. Sci Total Environ. 2018;616–617:1056–65. https://doi.org/10.1016/j.scitotenv.2017.10.213.
39. Schnepf U, Von Moers-Meßmer MAL, Brümmer F. A practical primer for image-based particle measurements in microplastic research. Microplastics Nanoplastics. 2023;3:16. https://doi.org/10.1186/s43591-023-00064-4.
40. Peneva S, Le QNP, Munhoz DR, Wrigley O, Wille F, Doose H, et al. Microplastic analysis in soils: a comparative assessment. Ecotoxicol Environ Saf. 2025;289:117428. https://doi.org/10.1016/j.ecoenv.2024.117428.
41. Möller JN, Heisel I, Satzger A, Vizsolyi EC, Oster SDJ, Agarwal S, et al. Tackling the challenge of extracting microplastics from soils: a protocol to purify soil samples for spectroscopic analysis. Environ Toxicol Chem. Volume 41. Oxford University Press (OUP); 2022;844–57. https://doi.org/10.1002/etc.5024.
42. Zhu Y, Wang S, Lv J, Yin J, Kong D. Study on the identification of microplastics in agricultural soils using segmented GASF combined with deep learning based on confocal micro-Raman spectroscopy. Measurement. 2025;256:118226. https://doi.org/10.1016/j.measurement.2025.118226.
43. Möller JN, Löder MGJ, Laforsch C. Finding microplastics in soils: a review of analytical methods. Environ Sci Technol Am Chem Soc (ACS). 2020;54:2078–90. https://doi.org/10.1021/acs.est.9b04618.
44. Dorau K, Hoppe M, Rückamp D, Köser J, Scheeder G, Scholz K, et al. Status quo of operation procedures for soil sampling to analyze microplastics. Microplastics Nanoplastics. 2023;3. https://doi.org/10.1186/s43591-023-00063-5.
45. Ivleva NP. Chemical analysis of microplastics and nanoplastics: challenges, advanced methods, and perspectives. Chem Rev Am Chem Soc. 2021;121:11886–936. https://doi.org/10.1021/acs.chemrev.1c00178.
46. Bläsing M, Amelung W. Plastics in soil: analytical methods and possible sources. Sci Total Environ. 2018;612:422–35. https://doi.org/10.1016/j.scitotenv.2017.08.086.
47. Lenz R, Enders K, Stedmon CA, Mackenzie DMA, Nielsen TG. A critical assessment of visual identification of marine microplastic using raman spectroscopy for analysis improvement. Mar Pollut Bull. 2015;100:82–91. https://doi.org/10.1016/j.marpolbul.2015.09.026.
48. Kalaronis D, Ainali NM, Evgenidou E, Kyzas GZ, Yang X, Bikiaris DN, et al. Microscopic techniques as means for the determination of microplastics and nanoplastics in the aquatic environment: a concise review. Green Anal Chem. 2022;3:100036. https://doi.org/10.1016/j.greeac.2022.100036.
49. Hurley RR, Lusher AL, Olsen M, Nizzetto L. Validation of a method for extracting microplastics from complex, organic-rich, environmental matrices. Environ Sci Technol. 2018;52:7409–17. https://doi.org/10.1021/acs.est.8b01517.
50. Pfohl P, Roth C, Meyer L, Heinemeyer U, Gruendling T, Lang C, et al. Microplastic extraction protocols can impact the polymer structure. Microplastics Nanoplastics. 2021. https://doi.org/10.1186/s43591-021-00009-9. 1.
51. Chouchene K, Nacci T, Modugno F, Castelvetro V, Ksibi M. Soil contamination by microplastics in relation to local agricultural development as revealed by FTIR, ICP-MS and pyrolysis-GC/MS. Environ Pollut. 2022;303:119016. https://doi.org/10.1016/j.envpol.2022.119016.
52. Dong M, Zhang Q, Xing X, Chen W, She Z, Luo Z. Raman spectra and surface changes of microplastics weathered under natural environments. Sci Total Environ. 2020;739:139990. https://doi.org/10.1016/j.scitotenv.2020.139990.
53. Rezaei M, Abbasi S, Pourmahmood H, Oleszczuk P, Ritsema C, Turner A. Microplastics in agricultural soils from a semi-arid region and their transport by wind erosion. Environ Res. 2022;212:113213. https://doi.org/10.1016/j.envres.2022.113213.
54. Ding L, Zhang S, Wang X, Yang X, Zhang C, Qi Y, et al. The occurrence and distribution characteristics of microplastics in the agricultural soils of Shaanxi Province, in north-western China. Sci Total Environ. 2020;720:137525. https://doi.org/10.1016/j.scitotenv.2020.137525.
55. Yu Y, Flury M. How to take representative samples to quantify microplastic particles in soil? Sci Total Environ. 2021;784:147166. https://doi.org/10.1016/j.scitotenv.2021.147166.
56. Coleman BR. An introduction to machine learning tools for the analysis of microplastics in complex matrices. Environ Sci Process Impacts Royal Soc Chem. 2025;27:10–23. https://doi.org/10.1039/D4EM00605D.
57. Hufnagl B, Stibi M, Martirosyan H, Wilczek U, Möller JN, Löder MGJ, et al. Computer-assisted analysis of microplastics in environmental samples based on µFTIR imaging in combination with machine learning. Environ Sci Technol Lett Am Chem Soc. 2022;9:90–5. https://doi.org/10.1021/acs.estlett.1c00851.
58. Hufnagl B, Steiner D, Renner E, Löder MGJ, Laforsch C, Lohninger H. A methodology for the fast identification and monitoring of microplastics in environmental samples using random decision forest classifiers. Anal Methods Royal Soc Chem (RSC). 2019;11:2277–85. https://doi.org/10.1039/c9ay00252a.
59. Plastics Europe. Plastics – the fast facts 2023, Plastics Europe. 2023; https://plasticseurope.org/knowledge-hub/plastics-the-fast-facts-2023/. Accessed 19 Oct 2025.
60. Hartmann NB, Hüffer T, Thompson RC, Hassellöv M, Verschoor A, Daugaard AE, et al. Are we speaking the same language? Recommendations for a definition and categorization framework for plastic debris. Environ Sci Technol Am Chem Soc. 2019;53:1039–47. https://doi.org/10.1021/acs.est.8b05297.
61. Gunn W, Torkian B. GitHub - torkian/vk4-python-driver. 2018; https://github.com/torkian/vk4-python-driver. Accessed 25 Sep 2025.
62. Senge JF, Astaraee AH, Dłotko P, Bagherifard S, Bosbach WA. Extending conventional surface roughness ISO parameters using topological data analysis for shot peened surfaces. Sci Rep. 2022;12:5538. https://doi.org/10.1038/s41598-022-09551-9.
63. Liebovitch LS, Toth T. A fast algorithm to determine fractal dimensions by box counting. Phys Lett A. 1989;141:386–90. https://doi.org/10.1016/0375-9601(89)90854-2.
64. Koenderink JJ, Van Doorn AJ. Surface shape and curvature scales. Image Vis Comput. 1992;10:557–64. https://doi.org/10.1016/0262-8856(92)90076-F.
65. Rousseeuw PJ. Silhouettes: a graphical aid to the interpretation and validation of cluster analysis. J Comput Appl Math. 1987;20:53–65. https://doi.org/10.1016/0377-0427(87)90125-7.
66. Magdziak H. RPubs - clustering properties using different methods. 2023; https://rpubs.com/av1ze/clustering. Accessed 26 Sep 2025.
67. Schindelin J, Arganda-Carreras I, Frise E, Kaynig V, Longair M, Pietzsch T, et al. Fiji: an open-source platform for biological-image analysis. Nat Methods Nat Publishing Group. 2012;9:676–82. https://doi.org/10.1038/nmeth.2019.
68. Arzt M, Deschamps J, Schmied C, Pietzsch T, Schmidt D, Tomancak P, et al. LABKIT: labeling and segmentation toolkit for big image data. Front Comput Sci Front. 2022;4. https://doi.org/10.3389/fcomp.2022.777728.
69. Anaconda. Anaconda software distribution. Computer software. Vers. 2-4.2.2. 2016; https://anaconda.com. Accessed 28 Sep 2025.
70. Pedregosa F, Varoquaux G, Gramfort A, Michel V, Thirion B, Grisel O, et al. Scikit-learn: machine learning in python. J Mach Learn Res. 2011;12:2825–30.
71. van der Walt S, Schönberger JL, Nunez-Iglesias J, Boulogne F, Warner JD, Yager N, et al. scikit-image: image processing in python. PeerJ PeerJ Inc. 2014;2. https://doi.org/10.7717/peerj.453.
72. Virtanen P, Gommers R, Oliphant TE, Haberland M, Reddy T, Cournapeau D, et al. SciPy 1.0: fundamental algorithms for scientific computing in python. Nat Methods Nat Publishing Group. 2020;17:261–72. https://doi.org/10.1038/s41592-019-0686-2.

73. Harris CR, van der Millman KJ, Gommers R, Virtanen P, Cournapeau D, et al. Array programming with NumPy. Nat Nat Publishing Group. 2020;585:357–62. https://doi.org/10.1038/s41586-020-2649-2.
74. Pandas. pandas-dev/pandas: pandas. 2020; https://doi.org/10.5281/zenodo.15831829
75. Amelung W, Zech W. Minimisation of organic matter disruption during particle-size fractionation of grassland epipedons. Geoderma. 1999;92:1–2. https://doi.org/10.1016/S0016-7061(99)00023-3.
76. Büks F, van Schaik NL, Kaupenjohann M. What do we know about how the terrestrial multicellular soil fauna reacts to microplastic? SOIL. Copernicus GmbH. 2020;6:245–67. https://doi.org/10.5194/soil-6-245-2020.
77. Büks F, Kaupenjohann M. Global concentrations of microplastics in soils – a review. SOIL. 2020;6:649–62. https://doi.org/10.5194/soil-6-649-2020.
78. Wrigley O, Braun M, Amelung W. Global soil microplastic assessment in different land-use systems is largely determined by the method of analysis: a meta-analysis. Sci Total Environ. 2024;957:177226. https://doi.org/10.1016/j.scitotenv.2024.177226.
79. Hu J, He D, Zhang X, Li X, Chen Y, Wei G, et al. National-scale distribution of micro(meso)plastics in farmland soils across China: implications for environmental impacts. J Hazard Mater Elsevier B V. 2022;424. https://doi.org/10.1016/j.jhazmat.2021.127283.
80. Xu L, Xu X, Li C, Li J, Sun M, Zhang L. Is mulch film itself the primary source of meso- and microplastics in the mulching cultivated soil? A preliminary field study with econometric methods. Environ Pollut. 2022;299:118915. https://doi.org/10.1016/j.envpol.2022.118915.
81. Meng F, Fan T, Yang X, Riksen M, Xu M, Geissen V. Effects of plastic mulching on the accumulation and distribution of macro and micro plastics in soils of two farming systems in northwest China. PeerJ. PeerJ Inc.; 2020. p. 8. https://doi.org/10.7717/peerj.10375.
82. van Schothorst B, Beriot N, Lwanga EH, Geissen V. Sources of light density microplastic related to two agricultural practices: the use of compost and plastic mulch. Environments. 2021;8. https://doi.org/10.3390/environments8040036.
83. Wang K, Min W, Flury M, Gunina A, Lv J, Li Q, et al. Impact of long-term conventional and biodegradable film mulching on microplastic abundance, soil structure and organic carbon in a cotton field. Environ Pollut. 2024;356:124367. https://doi.org/10.1016/j.envpol.2024.124367.
84. Rezaei M, Riksen MJPM, Sirjani E, Sameni A, Geissen V. Wind erosion as a driver for transport of light density microplastics. Sci Total Environ. 2019;669:273–81. https://doi.org/10.1016/j.scitotenv.2019.02.382.
85. Liu M, Song Y, Lu S, Qiu R, Hu J, Li X, et al. A method for extracting soil microplastics through circulation of sodium bromide solutions. Sci Total Environ. 2019;691:341–7. https://doi.org/10.1016/j.scitotenv.2019.07.144.
86. Huang Y, Liu Q, Jia W, Yan C, Wang J. Agricultural plastic mulching as a source of microplastics in the terrestrial environment. Environ Pollut. 2020;260:114096. https://doi.org/10.1016/j.envpol.2020.114096.
87. Beriot N, Peek J, Zornoza R, Geissen V, Huerta Lwanga E. Low density-microplastics detected in sheep faeces and soil: a case study from the intensive vegetable farming in southeast spain. Sci Total Environ. 2021;755:142653. https://doi.org/10.1016/j.scitotenv.2020.142653.
88. Pfohl P, Roth C, Wohlleben W. The power of centrifugation: how to extract microplastics from soil with high recovery and matrix removal efficiency. MethodsX. 2024;12:102598. https://doi.org/10.1016/j.mex.2024.102598.
89. Scopetani C, Chelazzi D, Mikola J, Leiniö V, Heikkinen R, Cincinelli A, et al. Olive oil-based method for the extraction, quantification and identification of microplastics in soil and compost samples. Sci Total Environ. 2020;733:139338. https://doi.org/10.1016/j.scitotenv.2020.139338.
90. Steiner T, Leitner L-C, Zhang Y, Möller JN, Löder MGJ, Greiner A, et al. Detection and specific chemical identification of submillimeter plastic fragments in complex matrices such as compost. Sci Rep. 2024;14:2282. https://doi.org/10.1038/s41598-024-51185-6.
91. Tsironi I, Schlesinger D, Späh A, Eriksson L, Segad M, Perakis F. Brine rejection and hydrate formation upon freezing of NaCl aqueous solutions. Phys Chem Chem Phys. 2020;22:7625–32. https://doi.org/10.1039/C9CP05436G.

Publisher's note